Interacting passive advective scalars in an active medium

Sk Raj Hossein

Raman Research Institute, Bangalore 560080, India

Rituparno Mandal and Madan Rao[*]

Simons Centre for the Study of Living Machines, National Centre for Biological Sciences (TIFR), Bellary Road, Bangalore 560065, India

Recent experimental studies, both *in vivo* and *in vitro*, have revealed that membrane components that bind to the cortical actomyosin meshwork are driven by active fluctuations, whereas membrane components that do not bind to cortical actin are not. Here we study the statistics of density fluctuations and dynamics of particles advected in an active *quasi*-two-dimensional medium comprising self-propelled filaments with no net orientational order, using a combination of agent-based Brownian dynamics simulations and analytical calculations. The particles interact with each other and with the self-propelled active filaments via steric interactions. We find that the particles show a tendency to cluster and their density fluctuations reflect their binding to and driving by the active filaments. The late-time dynamics of tagged particles is diffusive, with an *active diffusion* coefficient that is independent of (or at most weakly dependent on) temperature at low temperatures. Our results are in qualitative agreement with the experiments mentioned above. In addition, we make predictions that can be tested in future experiments.

I. INTRODUCTION AND MOTIVATION

The spatial organization, clustering, and dynamics of many cell surface molecules is influenced by interaction with the actomyosin cortex [1–6], a thin layer of actin cytoskeleton and myosin motors, measured to be around 250 nm in HeLa cells [7], that is juxtaposed with the membrane bilayer. Although the ultrastructure of the cortical actin cytoskeleton is as yet poorly defined, there is growing evidence that it is composed simultaneously of dynamic filaments [3] and an extensively branched static meshwork [8]. The coupling of the membrane to these two types of actin configurations is expected to affect the dynamics and organization of membrane components, presumably in different ways.

A common feature of these cell surface proteins is that they can bind, directly or indirectly, to cortical actin. As a consequence, a variety of myosin motors that act on actin filaments at the cortex, can drive the local clustering and dynamics of these cell surface proteins. Mutations of these proteins that abrogate this actin binding capacity leave them unaffected by the dynamics of the actomyosin cortex [3,4]. Similarly, silencing myosin motor activity, renders the dynamics of these cell surface proteins normal and akin to their mutated counterpart [3,4]. A description of the cell surface as an *Active Composite* of a multicomponent, asymmetric bilayer juxtaposed with a thin cortical actomyosin layer (Fig. 1), appears to consistently explain the anomalous dynamical features of these proteins [1,3,4]. In these earlier studies [3,9], we had used a coarse-grained description, based on active hydrodynamics [10]. Recently, it has been shown that much

of this behavior is recapitulated in a minimal *in vitro* reconstitution of a supported bilayer in contact with a thin layer of short actin filaments and Myosin-II minifilaments, driven by the hydrolysis of ATP [11]. The success of this minimal setup motivates us to revisit our continuum hydrodynamic description from a more microscopic standpoint. Our present study is an agent-based Brownian dynamics simulation of a mixture of polar active filaments and passive particles which interact with each other [12,13]. Since the parameter space for exploration is large, we restrict our study here to the case where the density of filaments and particles is low (negligible filament overlap), and where there is no net orientational order.

For the present purposes, we schematically represent the Active Composite Cell Surface, as in Fig. 1. To enable a systematic study, we conceptually separate out the different architectures of actin at the cortex: (1) where the cortical layer consists of only short dynamic filaments described as an active fluid (the subject of the present paper) and (2) where the cortical layer consists of only long filaments forming a static mesh of characteristic mesh size $\xi \approx 52$ nm in FRSK cells [8,14] (which we take up in a later publication). In future, we will combine these configurations into a single model of the cortical actomyosin.

Our choice of Brownian dynamics simulations is motivated by experiments on tagged particle diffusion both on the cell surface and in the *in vitro* reconstitution. Molecules that bind to dynamic actin (passive molecules) are affected by the active fluctuations of actomyosin; their diffusion shows anomalous behavior strongly indicative of active driving. On the other hand, molecules that do not interact with actin (inert molecules), such as short chain lipids and proteins whose actin-binding domain has been mutated so as to abrogate their interaction with actin, do not show any influence of

———————
[*]madan@ncbs.res.in
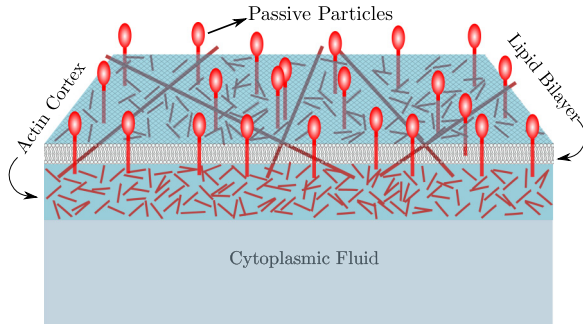
FIG. 1. Schematic of the Active Composite Cell Surface with a multicomponent asymmetric bilayer membrane juxtaposed with the cortical layer of actin and myosin. The actin layer consists of short dynamic actin and long static actin filaments, the latter forming a crosslinked mesh [8,14]. For clarity, myosin motors are not shown, the short filaments are active and represent myosin bound actin filaments. The passive molecules (shown in red) are transmembrane proteins that have a cytoplasmic actin-binding domain.

active fluctuations [3,4,11]. There appears to be no sign that the transport of these inert molecules is affected by potential hydrodynamic flows induced by active stresses coming from actomyosin [15,16].

While our primary motivation are the experimental studies of the tagged particle dynamics on the cell surface [3,4,11], our work is also relevant to transport in other living and nonliving systems, as long as the effects of hydrodynamics are negligible, for instance, to the movement of multiple motor-driven cargo vesicles or synthetic beads on the cytoskeletal network [17].

II. BROWNIAN DYNAMICS AND CHARACTERIZATION

A. Simulation details

We study the dynamics of a mixture of polar active filaments and passive particles using an agent-based Brownian dynamics simulation. The passive particles are modeled as monodisperse soft spheres of diameter σ. A pair of passive particles separated by a distance r interact via a truncated Lennard-Jones (LJ) pair potential of the form

$$V_{pp}(r) = 4\epsilon\left[\left(\frac{\sigma}{r}\right)^{12} - \left(\frac{\sigma}{r}\right)^6\right] + V_0 + V_2 r^2 \quad \text{for} \quad r \leqslant r_c$$
$$= 0 \quad \text{for} \quad r > r_c, \tag{1}$$

where $r_c = 2.5\sigma$ and values of V_0 and V_2 are chosen so that the potential and force are continuous at the truncation point. We set $\sigma = 1$ and $\epsilon = 1$ to be the units of length and energy, respectively.

The polar filaments are modeled as semiflexible bead-spring polymers, with both stretch and bend distortions [18,19]. We implement excluded volume interaction between the beads of same filament, as well as between two different filaments through a truncated Lennard-Jones pair potential of the form

$$V_{bb}(r) = 4\epsilon'\left[\left(\frac{\sigma'}{r}\right)^{12} - \left(\frac{\sigma'}{r}\right)^6\right] + V_0' + V_2' r^2 \quad \text{for} \quad r \leqslant r_c'$$
$$= 0 \quad \text{for} \quad r > r_c', \tag{2}$$

where r is the distance between the centers of the corresponding beads, and $r_c' = 2^{1/6}\sigma'$ and V_0', V_2' are constants, chosen so that the potential and force are continuous at r_c'. We take $\sigma' = 2$ and $\epsilon' = 1$. Each filament is composed of 10 beads and therefore has an equilibrium length $l_0 = 20$, in units of σ.

Note that with our choice of cutoffs, the particle-particle interaction V_{pp} has both attractive and repulsive parts, whereas the bead-bead interaction V_{bb} is strictly repulsive.

To make the filament semiflexible, we impose additional spring forces on the beads. A harmonic stretching potential with extensile stiffness $K_c = 400$, in units of ϵ/σ^2, ensures that the length of the filament does not deviate significantly from its equilibrium value, $l_0 = 20$. The bending energy of a triplet of connected beads is also harmonic in the angle, with a bending stiffness $K_b = 600$, in units of ϵ. This high K_b makes the filaments very stiff, with a typical persistence length much larger than l_0.

A propulsion force $\mathbf{f} = f_0\hat{\mathbf{n}}$ is imposed on each of the beads, along the average direction ($\hat{\mathbf{n}}$) of all the bonds present in a filament. Note that we do not impose any filament alignment rule nor do we prescribe any activity decorrelation time. Instead, these originate from thermal fluctuations on the constituent monomers comprising each filament and collisions driven by thermal and active forces, an emergent many-particle feature. As a consequence, both the local alignment and orientational decorrelation time are functions of temperature, density, and activity.

On the other hand, the passive particles are subject to thermal noise and can bind and unbind to the beads of the filament. The interactions between the beads of the filament and the passive particles are modeled by a harmonic potential of spring constant $K_s = 50$ in units of ϵ/σ^2. The harmonic potential is truncated at a cutoff distance $r_0 = 1$ and set to zero beyond it. When a passive particle comes within a distance r_0 from the center of a filament bead, it binds to the corresponding bead and gets advected along with the filament, under the application of propulsion force $f_0\hat{\mathbf{n}}$. The unbinding of the passive particle from the filament is facilitated by thermal noise. We will later characterize the binding and unbinding rates as a function of K_s and temperature. Note that we do not include any steric interaction between the passive particles on the membrane and the filaments in the cortex. A schematic showing the dynamic processes is displayed in Fig. 2(a).

Unless mentioned otherwise, all results presented here are for $N_p = 800$ passive particles and $N_r = 50$ self-propelled filaments in a two-dimensional (2D) area of linear dimension $L = 396.4$ with periodic boundary conditions. For most of the study, we take the area fractions of the filaments (c) and particles (ρ) to be $c = 0.01$ and $\rho = 0.004$, respectively.

The Brownian dynamics equations involve an update of both the passive particle and the filament bead coordinates, for which we have used a simple Euler integration scheme with integration time step $\Delta t \sim 10^{-4}$. The dynamics of the position of the ith passive particle is given by

$$\dot{\mathbf{r}}_i^p = \begin{cases} -\gamma_p^{-1}\nabla_i V_p + \sqrt{2k_B T/\gamma_p}\,\boldsymbol{\xi}_i, & \text{(unbound)} \\ -\gamma_p^{-1}\nabla_i V_p + \sqrt{2k_B T/\gamma_p}\,\boldsymbol{\xi}_i + \mathbf{f}_i/\gamma_p, & \text{(bound)} \end{cases}, \tag{3}$$
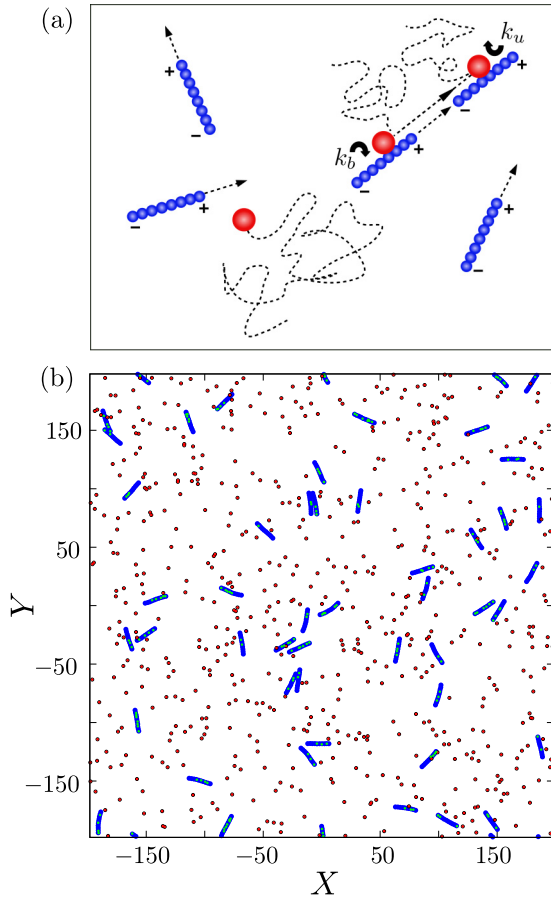
FIG. 2. (a) Schematic of the agent-based model, where the polar filaments (indicated by $\pm$) built from beads (blue) propel in a 2D background of passive particles (red). The passive particles can bind to the filaments with rate k_b and are advected with it. Upon unbinding with rate k_u, the passive particles undergo simple thermal diffusion. (b) Simulation snapshot showing self-propelled filaments (blue) and bound (green) and unbound (red) passive particles within a 2D box with periodic boundary conditions.

where γ_p is the friction coefficient of the passive particle, and V_p is the net potential felt by the ith passive particle and includes contributions from Eq. (1) and the bead-particle spring interactions. The diffusion of the unbound particle is driven by a thermal noise $\boldsymbol{\xi}_i$ with zero mean and unit variance acting on ith particle (k_B is the Boltzmann constant). On the other hand, the bound particles are subject to both the thermal noise and active driving.

The dynamics of the filament-bead displacements in our simulation is

$$\dot{\mathbf{r}}_j^b = -\gamma_b^{-1}\boldsymbol{\nabla}_j V_b + \sqrt{2k_B T/\gamma_b}\,\boldsymbol{\xi}_j + \mathbf{f}_j/\gamma_b, \qquad (4)$$

where γ_b is the friction coefficient of the bead, and V_b is the net potential felt by the jth bead and includes contributions from Eq. (2), harmonic stretching, and bending interactions. Since our study is entirely in the isotropic phase of the filaments, we have ignored complications that would arise by considering anisotropies in *both* friction and thermal noise, as required by detailed balance.

We take $\gamma_p = 1$, which together with $\sigma = 1$ and $\epsilon = 1$, sets the units of space, time, and energy. All other quantities can

TABLE I. Conversion between simulation units (S.U.) and real units (R.U.).

Parameter [Dimension]	S.U.	R.U.
σ [l]	1	10 nm
ϵ [ml^{2}t^{-2}]	1	4.14×10^{-21} J
γ_p [mt^{-1}]	1	$0.123\,\mathrm{pN}\,\mu\mathrm{m}^{-1}$ s
T [k]	1	300 K
t [t]	1	3×10^{-3} s
k_u, k_b [t^{-1}]	1	$333\,\mathrm{s}^{-1}$
f_0 [mlt^{-2}]	1	0.41 pN
V_a [lt^{-1}]	1	$3.3\,\mu\mathrm{m}\,\mathrm{s}^{-1}$
K_c [mt^{-2}]	1	$41.4\,\mathrm{pN}\mu\mathrm{m}^{-1}$
K_b [ml^{2}t^{-2}]]	1	4.14×10^{-21} J
K_s [mt^{-2}]	1	$41.4\,\mathrm{pN}\mu\mathrm{m}^{-1}$
D [l^{2}t^{-1}]	1	$3.3 \times 10^{-2}\,\mu\mathrm{m}^2/\mathrm{s}$

be written in terms of these units, so as to make Eqs. (3) and (4) dimensionless. In all that follows below, except in Sec. V, we have taken $\gamma_b = \gamma_p$. A typical snapshot of the agent-based simulation is shown in Fig. 2(b).

To be able to make contact with the *in vitro* reconstitution experiments [11], we translate our simulation units (S.U.) to real units (R.U.). Setting $\sigma = 10$ nm, $\gamma_b = 0.123$ pN μm^{-1} s [20] and $\epsilon = 4.14 \times 10^{-21}$ J, we can convert our simulation units to real units, as displayed in Table I. Note, however, that if we were to compare our simulation results with some other experimental system (e.g., an appropriately designed active colloidal suspension), then we would have to use a different conversion factor. To allow for this, we have varied the dimensionless temperature over the range $T = 0.25$–10 and the dimensionless propulsion force over the range $f_0 = 0$–4.0. We have typically run the Brownian dynamics simulation for a total time $t \sim 10^4$, ensuring that the system has reached steady state. Our initial conditions are chosen from a thermal distribution at temperature T, and all results presented here are averaged over 16 such independent realizations.

B. Statistics of filament orientation

We characterise the ith filament by its center of mass position $\mathbf{r}_i$ and a unit vector $\mathbf{n}_i = (\cos\theta_i, \sin\theta_i)$ along its long axis to describe its polar orientation (recall that the filaments are very stiff). We first ensure that the configuration of filaments is in the spatially homogeneous, orientationally isotropic state; this is demonstrated in the plots of the probability distribution of the polar $P(\theta)$ and nematic orientations $P(\tilde{\theta})$ (Fig. 3).

We then calculate the orientational correlation lengths, so as to ensure that this is much smaller than our system size and comparable to the size of the filaments. To do this, we calculate the spatial correlations of both the polar and nematic orientation,

$$C_P(r) = \left\langle \frac{1}{N^2} \sum_{i=1}^{N} \sum_{j=1}^{N} \cos(\theta_i - \theta_j) \right\rangle \qquad (5)$$

$$C_N(r) = \left\langle \frac{1}{N^2} \sum_{i=1}^{N} \sum_{j=1}^{N} [2\cos^2(\theta_i - \theta_j) - 1] \right\rangle, \qquad (6)$$
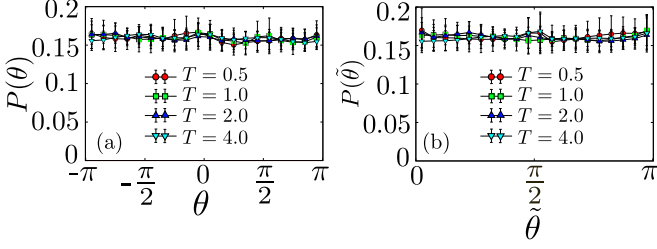
FIG. 3. Normalized distribution of (a) polar orientation $P(\theta)$ and (b) nematic orientation $P(\tilde{\theta})$, of the filaments at different temperature T with activity $f_0 = 4.0$, showing that the system is in the isotropic phase for a representative set of parameters. Data displayed with standard deviations over 16 independent realizations.

where $r = |\mathbf{r}_i - \mathbf{r}_j|$ is the distance between the center-of-mass of the ith and jth filaments. By fitting this to an exponential (Figs. 4 and 5), we extract the polar and nematic orientation correlation lengths, ζ_P and ζ_N, whose dependence on the area fraction of filaments c (we will henceforth refer to this as filament density) is shown in the inset.

Throughout the paper (unless mentioned otherwise) we work at a filament density of $c = 0.01$ and temperatures $T \geqslant 0.5$; in this regime, the orientational correlation lengths are of the order of the filament length, l_0, and hence comfortably within the isotropic phase.

C. Statistics of binding-unbinding of passive particles onto filaments

The dynamical Eqs. (3) and (4) are written entirely in terms forces, either active or derived from a potential, and thermal noise. The particles experience a binding and unbinding onto the filaments which depend on this interplay between thermal noise and the attractive potentials. Thus, for instance, the unbound passive particles diffuse in the 2D medium and ever so often come within the vicinity ($r \leqslant r_0 = 1$) of a moving filament bead, whereupon they bind to the filament bead. In the low-density limit, we expect the binding rate k_b to be
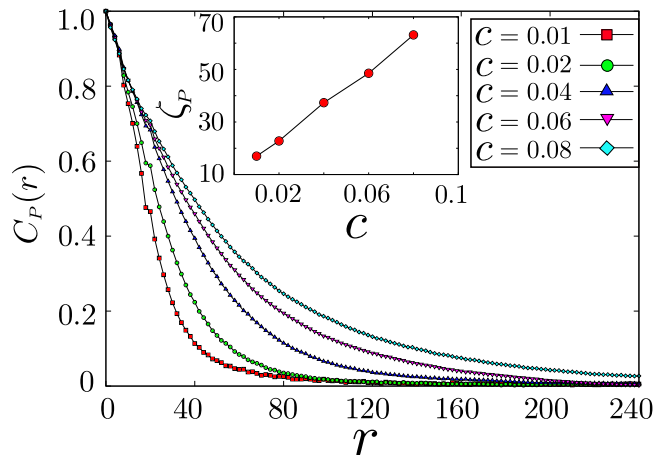
FIG. 4. Spatial correlation of the polar orientation, $C_P(r)$, of the filaments at different filament densities c at $T = 0.5$ and active propulsion $f_0 = 4$. Inset shows the corresponding correlation length ζ_P as a function of filament density c.
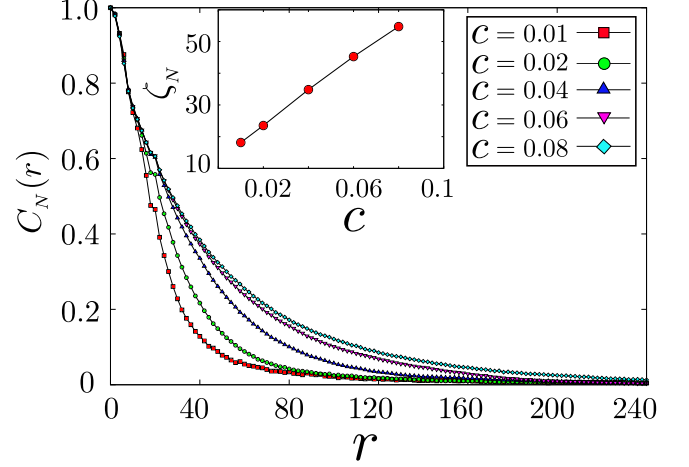
FIG. 5. Spatial correlation of the nematic orientation, $C_N(r)$, of the filaments at different filament density c at $T = 0.5$ and $f_0 = 4$. Inset shows the corresponding correlation length ζ_N as a function of filament density c.

diffusion limited and so $k_b \propto T$ and independent of K_s where K_s is the strength of trapping harmonic interaction.

To study the unbinding of a particle bound from a filament bead, we compute the rate of escape of a particle trapped in a truncated attractive harmonic potential [21], parametrized by K_s and r_0. This is given by

$$k_u = \frac{K_s^2 r_0^2}{\gamma_p k_B T} \exp\left(-\frac{K_s r_0^2}{2 k_B T}\right) \qquad (7)$$

and should be a good description of the dynamics of unbinding of the passive particles in the limit of low particle density.

We compare these theoretical estimates with the results of simulations on a mixture of particles and filaments at equilibrium (no active propulsion), from which we extract the values of k_u and k_b in two different ways. In the first method, we represent the stochastic binding and unbinding by a telegraphic process [22], characterized by a mean duty ratio,

$$\langle \phi \rangle = \frac{k_b}{k_b + k_u}, \qquad (8)$$

the fraction of time spent by the tagged particle in the bound state over the observation time, and a two-point correlator,

$$\langle \phi(t)\phi(t') \rangle = \langle \phi \rangle^2 + \langle \phi \rangle (1 - \langle \phi \rangle) e^{-2\frac{|t-t'|}{t_{sw}}}, \qquad (9)$$

where

$$t_{sw} = \frac{2}{k_b + k_u} \qquad (10)$$

is called the mean switching time and describes the mean time taken to switch from a bound to an unbound state. We calculate k_b and k_u, by fitting our simulation results to $\langle \phi \rangle$ and $\langle \phi(t)\phi(t') \rangle$. In the second method, we calculate k_u (k_b) directly, from the inverse mean time that the particle stays bound (unbound) on the filament.

Up to a scaling by a constant, the two numerical methods show identical variation as a function of temperature T and particle-filament binding potential K_s. These in turn agree with our analytical estimates, with no fit parameter (Fig. 6).
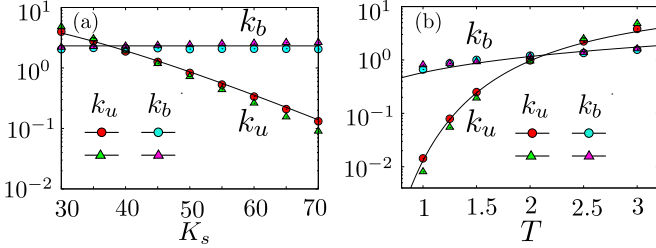
FIG. 6. Dependence of binding (unbinding) rates k_b (k_u) on (a) the strength of the particle-filament binding potential, K_s, and (b) temperature, T, calculated using the two different numerical methods (filled symbols) discussed in the text. These can be fit, with no undetermined parameter, to the analytic forms (solid lines) discussed in the text [Eq. (7)].

It is important that we do not *prescribe* the binding-unbinding rates; rather we derive them from the assigned potentials. The binding-unbinding rates thus depend nontrivially on temperature; they would also depend on the density of passive particles and filaments in the high-density limit. This will be crucial to our estimation of the tagged particle diffusion coefficient and its comparison with experimental data (Sec. IV B).

III. DENSITY FLUCTUATIONS OF PASSIVE ADVECTIVE SCALARS IN AN ACTIVE MEDIUM

We now study the statistics of density fluctuations and dynamics of the actively driven passive particles. We find that the active driving tends to cluster the passive particles; this shows up in the two-point spatial density correlation function and the statistics of the density fluctuations.

A. Radial distribution function

We study the behavior of the radial distribution function of the passive particles $g(r)$,

$$g(r) = \frac{1}{N_p \rho} \left\langle \sum_i \sum_{i \neq j} \delta(r - |\mathbf{r_i} - \mathbf{r_j}|) \right\rangle, \qquad (11)$$

where N_p is the total number of passive particles and ρ the passive particle density. When $k_b = 0$ and $f_0 = 0$, i.e., when the particles do not bind to the filament (inert particles) and there is no propulsion force, $g(r)$ has the form of a dilute fluid (Fig. 7). When we allow for particle binding, but in the absence of propulsion force, the $g(r)$ displays oscillations, which arise from particles binding to periodic locations on the filaments (Fig. 7); note that $r = 20$ coincides with the filament length. In this equilibrium situation, the particles not bound to the filaments do not show any clustering. We now consider the case when the filaments are driven by a propulsion force f_0. We see that the propulsion drives the clustering of the filaments, which in turn leads to an increase in correlation between bound particles, even at distances beyond the filament length (Fig. 7).

B. Probability distribution of local number density

This activity induced clustering of the passive particles should be reflected in the probability distribution of the excess
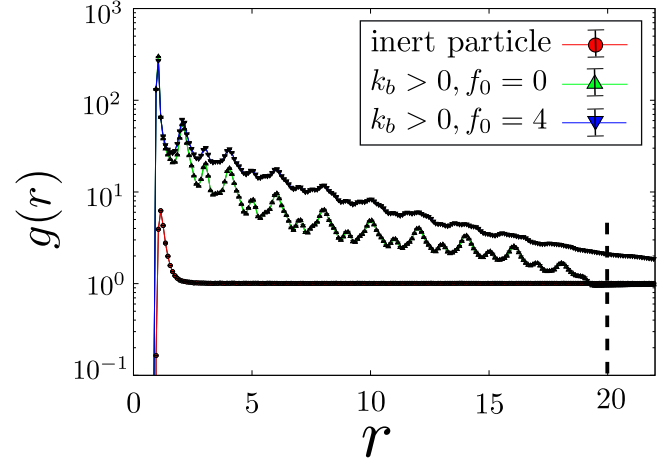
FIG. 7. Radial distribution function $g(r)$ for (1) equilibrium system of inert particles ($k_b = 0$: red ●), (2) equilibrium system of passive particles which can bind to the filaments ($k_b > 0$, $f_0 = 0$: green △), and (3) driven system of passive particles which can bind to the self-propelled filaments ($k_b > 0$, $f_0 = 4$: blue ▽). In the presence of activity the peak heights increase and $g(r)$ falls off more gradually, indicating a high degree of clustering of the bound particles, even at distances larger than the filament length. Data displayed with standard deviations over 16 independent realizations.

number density. To compute this we divide the system into blocks of size $\Omega = 39.64$ and count the number of passive particles n in each block, to obtain the steady state distribution $P(n)$.

The statistics of density fluctuations of inert particles, in the dilute limit (Fig. 8), are described by a probability
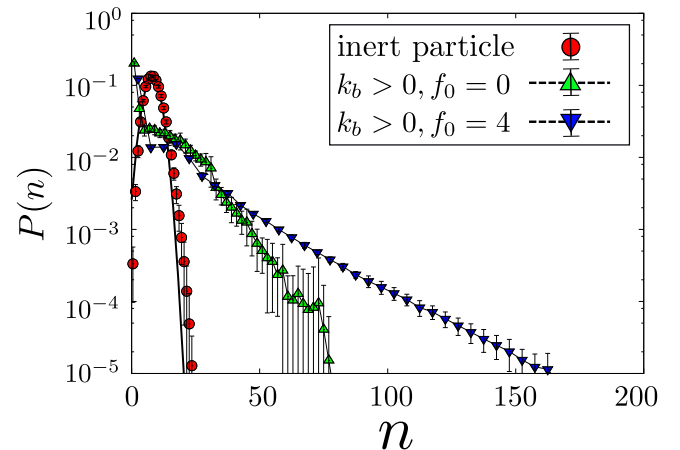
FIG. 8. Probability distribution of number density $P(n)$ for (1) equilibrium system of inert particles ($k_b = 0$: red ●), (2) equilibrium system of passive particles which can bind to the filaments ($k_b > 0$, $f_0 = 0$: green △), and (3) driven system of passive particles which can bind to the self-propelled filaments ($k_b > 0$, $f_0 = 4$: blue ▽). For inert particles, $P(n)$ fits the virial expression Eq. (12) (dark line) with a second virial coefficient, $B_2 = -0.99$. $P(n)$ picks up an exponential tail for particles that bind and unbind onto the filaments and moves towards the typical value as the active propulsion force gets larger. Data displayed with standard deviations over 16 independent realizations.

distribution that resembles a gas at temperature T and the average number of particle in the blocks $\bar{n}$, namely,

$$P(n) = \frac{1}{\sqrt{2\pi\sigma^2}} \exp\left[-\frac{(n-\bar{n})^2}{2\sigma^2}\right], \qquad (12)$$

where $\bar{n} = \Omega\rho$. We have taken the variance of the above distribution to have a virial form, $\sigma^2 = \bar{n} - \frac{2B_2}{\Omega}\bar{n}^2 + \cdots$; a fit to the numerical data gives $B_2 = -0.99$ (dark line in Fig. 8).

On the other hand, the probability distribution for passive particles picks up an exponential tail arising from the binding-unbinding statistics of the particles. This exponential tail gets more pronounced when the filaments are made active and moves towards the typical value as the active propulsion force gets larger (Fig. 8). This reflects the fact that for high driving, the typical particle is clustered. Both these results are consistent with the observed clustering of actin-binding proteins driven by actomyosin flows in the *in vitro* reconstitution system reported in Ref. [11].

C. Number fluctuations: Crossover from anomalous to Brownian

Note that the active system of filaments is in the isotropic phase, and we should not expect to see the giant number fluctuations normally associated with active systems with global-orientational order [23–25]. However, when we compute the root mean square fluctuations Δn and mean $\bar{n}$ of the number of passive particles over regions of ever increasing area, and plot them with respect to each other, we find that initially $\Delta n \propto \bar{n}^\alpha$ with $\alpha = 0.784$. Subsequently, as $\bar{n}$ increases, the variance scaling shows a crossover to $\alpha = 0.5$. This crossover occurs over a scale corresponding to the orientational correlation length, which can in principle be large, especially close to the isotropic-nematic transition or high f_0. This is especially apparent in the high-particle-density regime; see Fig. 9 for particle density $\rho = 0.05$ and filament density $c = 0.02$. This slow crossover explains the observed anomalous number fluctuations in the *in vitro* actomyosin reconstitution system [11]. In order to recover the crossover to the expected normal fluctuations at large n, one needs to probe over length scales larger than this crossover length [26].

IV. TRANSPORT OF PASSIVE ADVECTIVE SCALARS IN AN ACTIVE MEDIUM

We now study the transport of passive particles moving in the active medium. Because the filaments are orientationally disordered, the long time dynamics of the particles is always diffusive. However, the diffusion characteristics can change depending on the statistics of (un)binding to the active filaments.

A. Typical trajectories

The space-time trajectories of the passive particles show three qualitatively different behaviors. At very low temperatures compared to $\overline{U} = K_s r_0^2/4$, a passive particle once bound to a filament rarely unbinds, and hence gets advected with the self-propelled filament [Fig. 10(a)]. The direction of advection changes because of thermal fluctuations and collisions between filaments. Increasing the temperature increases the
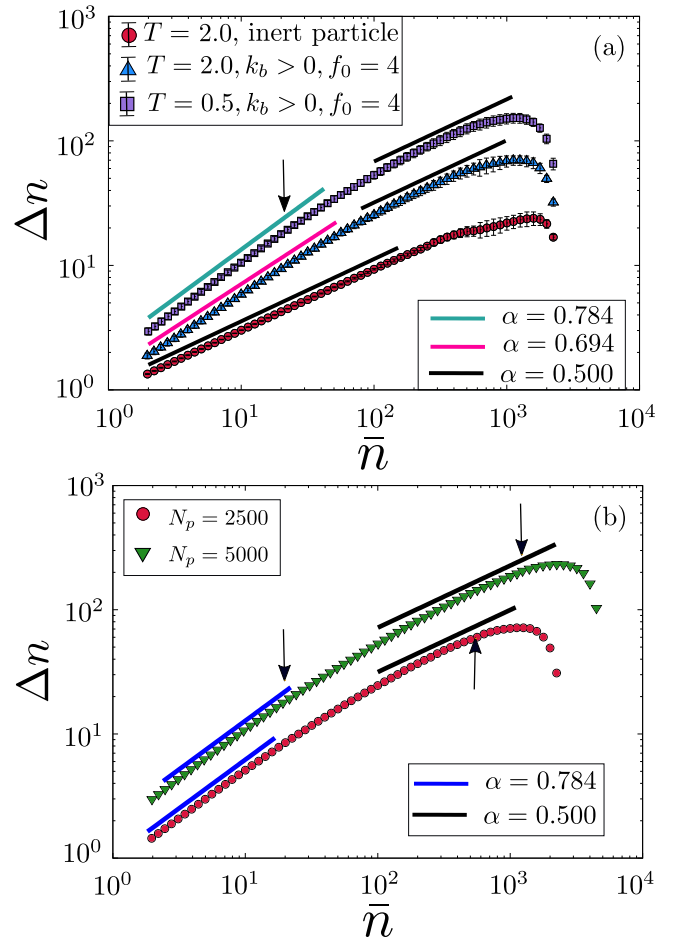
FIG. 9. (a) Root-mean-square fluctuations of the number of passive particles Δn versus the mean $\bar{n}$ for inert (red ●) and passive particles at two different temperatures, $T = 0.5$ (△) and $T = 2.0$ (□). Solid lines indicate the local slope α in this log-log plot of $\Delta n \propto \bar{n}^\alpha$. The values of α indicated in the legend show that while inert particles exhibit normal fluctuations ($\alpha = 0.5$), passive particles show large fluctuations at small $\bar{n}$ (with α depending on T and f_0) that crosses over to normal fluctuations beyond a scale corresponding to the orientational correlation length (indicated by the arrow). Data displayed with standard deviations over 16 independent realizations. (b) To study the crossover behavior, we plot Δn versus $\bar{n}$ for two different system sizes at $T = 0.5$. The crossover from $\alpha = 0.784$ to $\alpha = 0.5$ occurs at the orientational correlation length (arrow to the left), which being much smaller than system size, does not show any difference in the two system sizes. However, the eventual flattening and drop of the curve at large $\bar{n}$ is a system size effect, as seen by the arrows to the right. The $N_p = 2500$ data have been shifted along the y axis for better visualization.

probability of unbinding from the filament, whereupon the particle undergoes unrestricted thermal diffusion before binding again [Fig. 10(b)]. At even higher temperatures, $k_B T/\overline{U} \approx 1$ the particles do not bind to the filaments, and the motion is simple thermal diffusion [Fig. 10(c)].

B. Statistics of displacements and diffusion coefficient

Propensity distribution. The distribution of displacements Δx (along the $\hat{x}$ direction) evaluated over a time window t_w
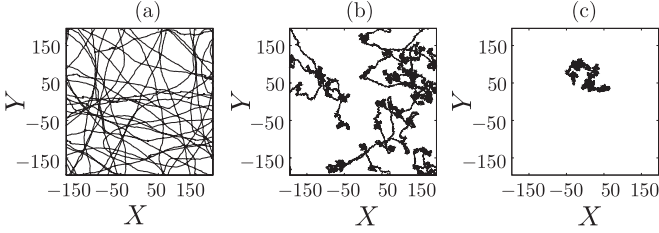
FIG. 10. Typical trajectories of passive particles for a fixed propulsion force $f_0 = 4.0$ at different temperatures: (a) $T = 0.5$ (low: $k_B T / \overline{U} = 0.04$), (b) $T = 4.0$ (intermediate: $k_B T / \overline{U} = 0.32$), and (c) $T = 10.0$ (high: $k_B T / \overline{U} = 0.8$).

is called the *propensity distribution*. This will depend on the statistics of binding and unbinding, which in turn depends on the temperature T and f_0, densities of filaments and particles, and of course on the time window t_w, which we fix at $t_w = 10$. This can be obtained both from our Brownian dynamics simulation and, in the dilute limit, analytically.

In the dilute limit, one can obtain the form of this probability distribution from the stationary process describing the particle vector displacements in a small time interval t_w,

$$\mathbf{r}(t_w) = \mathbf{r}(0) + \int_0^{t_w} \mathbf{V}(t') \, dt', \tag{13}$$

where $\mathbf{V}$ is the velocity of the tagged particle at time t, given by

$$\mathbf{V}(t) = \phi(t) \frac{f_0}{\gamma} \hat{\mathbf{n}}(t) + [1 - \phi(t)] \boldsymbol{\xi}(t), \tag{14}$$

where $\hat{\mathbf{n}}$ is the polar vector representing the orientation of the filament to which the particle is bound at time t, $\boldsymbol{\xi}$ is the thermal noise, and $\phi(t)$ is the telegraphic noise whose statistics is described in Sec. II C. The distribution of the particle displacements $\Delta x_{t_w} \equiv [(\mathbf{r}(t_w) - \mathbf{r}(0)] \cdot \hat{\mathbf{x}}$ can be obtained by evaluating

$$P(\Delta x) = \langle \delta(\Delta x - \Delta x_{t_w}) \rangle, \tag{15}$$

where Δx_{t_w} is obtained from Eq. (13) and the angular bracket denotes an average over the joint distribution of $\boldsymbol{\xi}$ and ϕ. This can be evaluated by standard techniques of Fourier transformation and cumulant expansion [22],

$$\ln \tilde{P}(k) = \sum_{m=1}^{\infty} \frac{(ik)^m}{m!} \langle (\Delta x_{t_w})^m \rangle_c, \tag{16}$$

where $\tilde{P}(k)$ is the Fourier transform of $P(\Delta x)$. The mth cumulants $\langle (\Delta x_{t_w})^m \rangle_c$ can be evaluated from Eqs. (13) and (14), knowing that ϕ and $\boldsymbol{\xi}$ are independent stochastic processes. The distribution $P(\Delta x)$ is then obtained by taking the inverse Fourier transform of $\tilde{P}(k)$.

However, in practice, the inverse Fourier transform of $\tilde{P}(k)$, for the stationary process Eq. (13), has to be evaluated numerically. Rather than do this, we provide an alternate argument which gives more insight.

At low enough T, the passive particles are completely bound to the self-propelled filaments, and so as long as $t_w < \tau$, the orientational correlation time of the filaments, the particles get displaced by $\Delta \mathbf{r} = \frac{f_0 t_w}{\gamma_p} \hat{\mathbf{n}}$, where γ_p is the
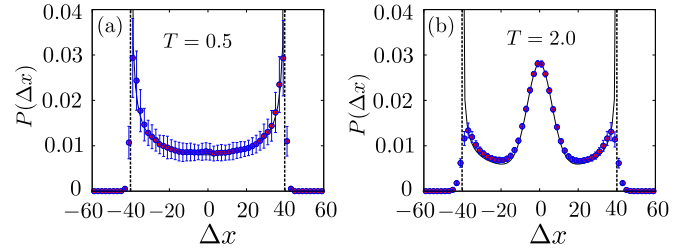
FIG. 11. Probability distribution $P(\Delta x)$ of the displacements of passive particles, evaluated for fixed time interval $\triangle t = 10$, at a propulsion force $f_0 = 4.0$ and temperatures (a) $T = 0.5$ and (b) $T = 2.0$. The central peak comes from the fraction undergoing thermal diffusion, while the side peaks come from the bound fraction undergoing active motion. The black filled line shows parameter-free fits to the approximate analytical form [Eq. (17)], where we have estimated the value of $\langle \phi \rangle = 0.9995$ at $T = 0.5$ (mainly bound) and $\langle \phi \rangle = 0.632$ at $T = 2.0$. Data displayed with standard deviations over 16 independent realizations.

friction coefficient and $\hat{\mathbf{n}}$ is the unit vector representing the average orientation of a filament during time interval t_w. Since the filament orientation is uniformly distributed, the contribution to the step-size distribution from this process is $P(\Delta x) = \frac{\gamma_p}{\pi f_0 t_w} \frac{1}{\sqrt{1 - (\frac{\gamma_p}{f_0} \frac{\Delta x}{t_w})^2}}$. On the other hand, at very high T, the particles are completely unbound and undergo thermal diffusion, for which the step-size distribution is $P(\Delta x) = \frac{1}{\sqrt{2\pi\sigma^2}} \exp\left[-\frac{(\Delta x)^2}{2\sigma^2}\right]$, where $\sigma^2 = \frac{2k_B T}{\gamma_p} t_w$. We propose that at an intermediate T, the propensity distribution can be written as a linear combination, weighted by the duty ratio $\langle \phi \rangle$:

$$P(\Delta x) = \frac{\gamma_p}{\pi f_0 t_w} \frac{\langle \phi \rangle}{\sqrt{1 - \left(\frac{\gamma_p}{f_0} \frac{\Delta x}{t_w}\right)^2}}$$
$$+ \frac{1 - \langle \phi \rangle}{\sqrt{2\pi\sigma^2}} \exp\left[-\frac{(\Delta x)^2}{2\sigma^2}\right]. \tag{17}$$

Considering that there are no undetermined parameters, the agreement of this approximate analytical form with the results of the Brownian simulation is quite reasonable; see Fig. 11.

Mean square displacement. From the statistics of the displacement we can compute the mean square displacement (MSD) as $\langle \Delta \mathbf{r}^2(t) \rangle = \langle \frac{1}{N_p} \sum_i |\mathbf{r}_i(t_0 + t) - \mathbf{r}_i(t_0)|^2 \rangle$, where $\mathbf{r_i}$ is the position of the ith particle. This shows a change from a short time diffusive regime crossing over to a long time diffusive regime via an intermediate superdiffusive regime [Fig. 12(a)]. We estimate the second crossover time $t_c(T, f_0)$ from the superdiffusive to late-time diffusion D, by fitting the simulation data to $\langle \Delta \mathbf{r}^2(t) \rangle = 4Dt \left[1 - \exp(-t/t_c)\right]$ [27], using which we can collapse the MSD data for different values of active propulsion f_0 [Fig. 12(b)]. From this we see that t_c decreases with f_0 [Fig. 12(b) inset]. This is because the filament orientation decorrelates on account of collisions, whose frequency increases with f_0. In experimental systems where hydrodynamics plays a crucial role [27], this dependence of t_c on f_0 may be different. In situations where the crossover t_c is large, the apparent superdiffusion behavior would last for many decades in time. We can then fit the MSD to $\langle \Delta \mathbf{r}^2(t) \rangle \sim t^\beta$ to obtain the superdiffusion exponent $\beta > 1$;
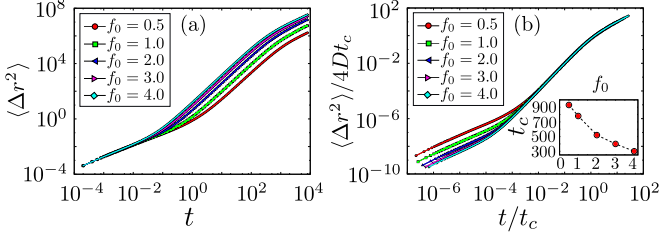
FIG. 12. (a) MSD of passive particles as a function of time at $T = 0.5$ for different values of self-propulsion force (f_0) of the filaments. (b) Collapse of MSD using crossover time (t_c) and long time diffusion constant for the same case. Inset shows crossover time (t_c) as a function of self-propulsion force (f_0) of the active filaments for the same case.

we find that $\beta = 1.95$ at $T = 0.5$ and $\beta = 1.77$ at $T = 2.0$, for a propulsion force $f_0 = 4.0$.

Temperature and activity dependence of MSD. We now compute the late-time diffusion coefficient of the tagged particles, $D = \lim_{t\to\infty}\langle\Delta \mathbf{r}^2(t)\rangle/4t$, for different T and f_0. For a fixed f_0, one might expect that at low temperatures D is weakly dependent on (or even independent of) temperature because a particle once bound to the filament remains so and undergoes *active diffusion* as it is transported by the filament (Fig. 13). As we increase the temperature, D decreases, since a particle spends less time, on an average, bound to the filament (recall we have set $\gamma_b = \gamma_p$). At high temperatures, the particles are predominantly unbound, and hence D resembles that of an inert particle, which increases linearly with temperature. This is indeed what we see from a direct numerical simulation of the Brownian dynamics trajectories of a tagged particle (Fig. 13).

From the stationary process, Eq. (13), the MSD of the tagged passive particle,

$$\langle\delta\mathbf{r}^2(t)\rangle = \int_0^t \int_0^t \langle\mathbf{V}(t')\cdot\mathbf{V}(t'')\rangle\, dt'\, dt'', \quad (18)$$
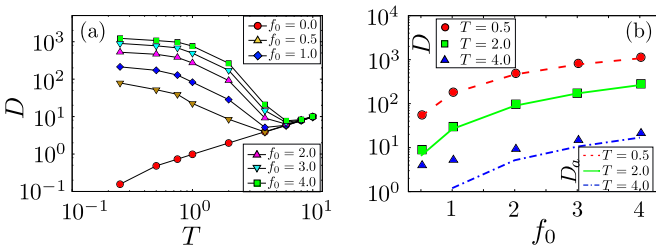
FIG. 13. (a) Diffusion coefficient (D) of tagged passive particles has been plotted as a function of T for different values of f_0 of the filaments. At the low-temperature regime D is weakly dependent on T (signature of *active diffusion*). At the intermediate regime D decreases then again increases at the high-temperature regime where thermal diffusion dominates. (b) Total diffusion coefficient D (with points) and *active diffusion coefficient D_a*(with line) with f_0 for different T. In the low-temperature and high-activity regime the difference between D and D_a is insignificant; as we increase T and decrease f_0 the difference becomes prominent.
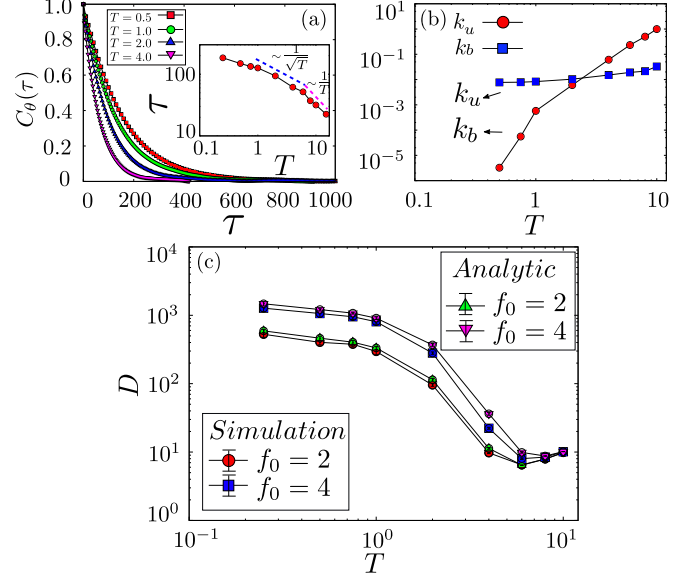
FIG. 14. (a) Temporal correlation of the direction of persistent movement of the filaments, measured by the velocity orientation correlation function $C_\theta(t)$, at different temperatures, with the filament density $c = 0.01$ and propulsion force $f_0 = 4$. Inset shows the corresponding orientation correlation time τ as a function of T. (b) Temperature dependence of binding (k_b) and unbinding (k_u) rates calculated from the statistics of the telegraphic noise $\phi(t)$. (c) Both simulation and analytic calculation of diffusion coefficient (D) of tagged passive particles are plotted as a function of temperature (T) for two different activities ($f_0 = 2, 4$) for filament density $c = 0.01$. Data displayed with standard deviations over 16 independent realizations. Note that the standard deviation in the analytic graph is because we have used the values of τ, k_u, and k_b from simulations.

immediately gives the diffusion coefficient,

$$D = \frac{1}{2}\int_0^\infty \langle\mathbf{V}(t)\cdot\mathbf{V}(0)\rangle\, dt. \quad (19)$$

Using Eq. (14), we see that the diffusion coefficient of the bound particle is given by the correlations of $\mathbf{V}_a$, which is given by [Fig. 14(a)],

$$\langle\mathbf{V}_a(t)\cdot\mathbf{V}_a(0)\rangle = \frac{f_0^2}{\gamma_p^2}\langle\cos[\theta(t) - \theta(0)]\rangle$$

$$= \frac{f_0^2}{\gamma_p^2}e^{-|t|/\tau}. \quad (20)$$

The diffusion coefficient can now be simply evaluated,

$$D = \frac{f_0^2 \tau k_b(\tau k_b + 1)}{2\gamma_p^2(k_u + k_b)[(k_u + k_b)\tau + 1]} + \frac{k_B T k_u}{\gamma_p(k_u + k_b)}. \quad (21)$$

To plot D versus T and f_0, we need to know the values of k_b, k_u (equivalently $\langle\phi\rangle$, t_{sw}) and τ, which depend on the temperature and density, and which we obtain from our simulations. We then compare this semianalytical form to the direct numerical computation of the diffusion coefficient from the Brownian dynamics trajectories (Fig. 14). The agreement between the two is excellent. Our computations recapitulate
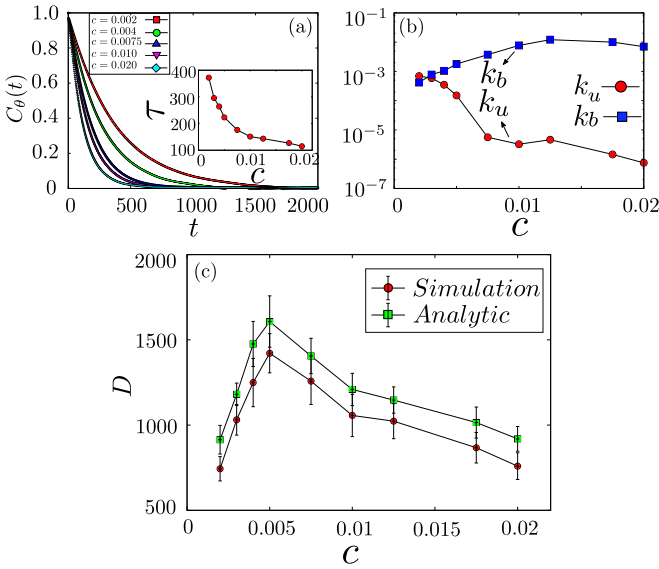
FIG. 15. (a) Temporal correlation of the direction of persistent movement of the filaments, measured by the velocity orientation correlation function $C_\theta(t)$, with different filament density (c), at temperature $T = 0.5$ and propulsion force $f_0 = 4$. Inset shows the corresponding orientation correlation time τ as a function of c. (b) Dependence of binding (k_b) and unbinding (k_u) rates on filament density c, calculated from the statistics of the telegraphic noise $\phi(t)$. (c) Both simulation and analytic calculation of diffusion coefficient (D) of tagged passive particles has been plotted as a function of filament density (c) at $T = 0.5$ and for $f_0 = 4$. Data displayed with standard deviations over 16 independent realizations. Note that the standard deviation in the analytic graph is because we have used the values of τ, k_u, and k_b from simulations.

in vivo observations of the temperature insensitivity of diffusion coefficient of a variety of passive molecules driven by actomyosin flows at the cell surface, using fluorescence correlation spectroscopy [4].

It might be objected that in our analysis we have treated the active propulsion as an independently tunable parameter, thus precluding the possibility that the activity itself may be temperature dependent. However, as we saw in Ref. [2], and as noted elsewhere [28,29], the actomyosin contractile processes taken as a whole appear to be independent of temperature in the physiological range, 24–37 °C.

Figure 15 shows the dependence of D on filament concentration c, both from direct simulations and from the analytical form using the values of k_b, k_u (equivalently $\langle \phi \rangle$, t_{sw}) and τ, from simulations. This shows optimal transport at a specific filament concentration; the orientational decorrelation time is smaller at higher filament concentration, due to higher collision frequency.

V. VISCOSITY STRATIFICATION AND ITS EFFECT ON MEMBRANE DIFFUSION

So far, our study of transport of passive molecules in an active medium has been restricted to two dimensions. However, as we discussed in Sec. I, the cell surface is a composite of a bilayer membrane and a thin actomyosin cortex. Thus while the proteins move on the cell membrane,
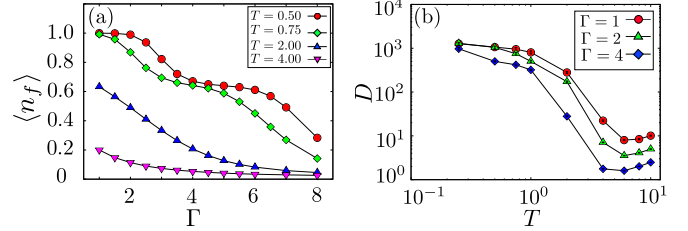
FIG. 16. (a) Fraction of bound particles $\langle n_b \rangle$ decreases with $\Gamma = \gamma_p/\gamma_b$ over a range of temperatures. (b) Diffusion coefficient versus temperature at different values of viscosity mismatch parameter Γ. In both figures, the propulsion force has been fixed at $f_0 = 4.0$.

the actively driven actin moves in the actomyosin cortex. The viscosities of these two layers are significantly different, with the bilayer membrane having a viscosity which is an order of magnitude larger than the cortex (≈ 0.86 Pa s [20]). Indeed the local viscosity of a multicomponent membrane can be quite heterogeneous; for instance, the particle mobility within the so-called "membrane rafts" or liquid-ordered regions on the cell membrane can be very different from those within liquid-disordered regions. Moreover the local cortical viscosity depends on local actin, myosin, and cross-linker concentrations. How does this viscosity mismatch affect the actively driven transport of passive molecules?

To address this important issue within our simulation, we vary the ratio of the friction coefficients $\Gamma = \gamma_p/\gamma_b$ in Eqs. (3) and (4). We find that the mean fraction of passive particles bound to filaments $\langle n_b \rangle$ decreases with increasing Γ over a range of T and $f_0 = 4.0$ [Fig. 16(a)]. This is an interesting observation, since one might have naively thought that $\langle n_b \rangle$ is solely governed by binding-unbinding, a purely equilibrium process and hence independent of relative viscosities. However, we see that the drag induced by the imposed viscosity stratification (a nonequilibrium feature) can "peel off" particles from the filaments. It is not clear to us why we see a shoulder at intermediate values of Γ for low enough temperatures [Fig. 16(a)].

This is reflected in changes that we observe in the measured diffusion coefficient D, as it decreases with increasing Γ at different T [Fig. 16(b)]. As can be seen, the active-diffusion regime at low temperatures becomes significantly more temperature dependent as the viscosity mismatch Γ increases.

The results of this section are not purely academic; on the contrary, taken together they pose an interesting possibility that by tuning local viscosity mismatch, for instance by locally recruiting the so-called "membrane rafts" or liquid-ordered regions on the cell membrane or by locally regulating the concentrations of actin, myosin, or cross-linkers, the living cell surface could control the clustering and transport of specific membrane proteins.

VI. DISCUSSION

We had earlier shown that a coarse-grained active hydrodynamics description of the active composite cell surface, successfully explains the statistics of clustering of membrane proteins capable of binding to the cortical actomyosin in living cells [1,3]. Such a description make predictions regarding the

statistics of density fluctuations and transport of such actin-binding membrane proteins, which were verified in experiments [3,4]. Following this we were able to recapitulate much of this behavior in a minimal *in vitro* system comprising a thin layer of short actin filaments and Myosin-II minifilaments on a supported bilayer [11]. The success of this approach has motivated us to do an agent-based Brownian dynamics simulation using these minimal ingredients: that of a collection of passive molecules which bind and unbind to actin filaments and move in this active medium in two dimensions.

The results obtained here, based on simulations and analytical calculations, are in qualitative agreement with the experiments both *in vivo* and *in vitro*. For instance, the exponential tails appearing in the probability distribution of the number (Fig. 8) and the scaling of the variance of the number (Fig. 9) is precisely the behavior seen in our earlier *in vitro* experiments. In addition, we show how activity-induced clustering of passive particles (Fig. 7) arises naturally from such a minimal description.

We have also studied transport of passive particles moving in this active medium and find that there is a crossover from an intermediate time superdiffusive to late-time diffusive behavior as a consequence of active driving [Fig. 12(a)]. The transport behavior shows a striking dependence on temperature and active forcing; at low temperatures the diffusion coefficient is insensitive to temperature and crosses over to a linear temperature dependence at higher temperatures, in qualitative agreement with experiments [4].

Finally, recognizing that the viscosity of the cortical layer is different from that of the membrane, we show that a friction coefficient mismatch has a strong effect on the mean number of bound particles and the diffusion coefficient. This is a consequence of the drag induced by the imposed viscosity stratification, which results in a "peeling off" of the particles from the filaments. This opens up the possibility of local tuning of viscosity mismatch, for instance, by locally recruiting the so-called "membrane rafts" or liquid-ordered regions on the cell membrane or by locally regulating the concentrations of actin, myosin, or cross-linkers. This could result in yet another mechanism by which the cell surface might locally control the clustering and transport of specific membrane proteins. We hope that some of these predictions can be tested in future experiments.

[1] M. Rao and S. Mayor, Curr. Op. Cell Biol. **29**, 126 (2014).

[2] D. Goswami *et al.*, Cell **135**, 18085 (2008).

[3] K. Gowrishankar, S. Ghosh, S. Saha, S. Mayor, and M. Rao, Cell **149**, 1353 (2012).

[4] S. Saha, I. Lee, A. Polley, J. T. Groves, M. Rao, and S. Mayor, Mol. Biol. Cell **26**, 4033 (2015).

[5] S. J. Plowman, C. Muncke, R. G. Parton, and J. F. Hancock, Proc. Natl. Acad. Sci. U. S. A. **102**, 15500 (2005).

[6] D. Lingwood and K. Simons, Science **327**, 46 (2010).

[7] P. Chugh, A. G. Clark, M. B. Smith, D. A. D. Cassani, K. Dierkes, A. Ragab, P. P. Roux, G. Charras, G. Salbreux, and E. K. Paluch, Nat. Cell Biol. **19**, 697 (2017).

[8] N. Morone *et al.*, J. Cell Biol. **174**, 851 (2006).

[9] K. Gowrishankar and M. Rao, Soft Matter **12**, 2040 (2016).

[10] M. C. Marchetti, J. F. Joanny, S. Ramaswamy, T. B. Liverpool, J. Prost, M. Rao, and R. A. Simha, Rev. Mod. Phys. **85**, 1143 (2013).

[11] D. V. Koster, K. Husain, E. Iljazi, A. Bhat, P. Bieling, R. D. Mullins, M. Rao, and S. Mayor, Proc. Natl. Acad. Sci. U. S. A. **113**, E1645 (2016).

[12] S. R. McCandlish, A. Baskaran, and M. F. Hagan, Soft Matter **8**, 2527 (2012).

[13] J. Stenhammar, R. Wittkowski, D. Marenduzzo, and M. E. Cates, Phys. Rev. Lett. **114**, 018301 (2015).

[14] T. Fujiwara, K. Ritchie, H. Murakoshi, K. Jacobson, and A. Kusumi, J. Cell Biol. **157**, 904 (2002).

[15] Y. Hatwalne, S. Ramaswamy, M. Rao, and R. A. Simha, Phys. Rev. Lett. **92**, 118101 (2004).

[16] A. Basu, J. F. Joanny, F. Julicher, and J. Prost, New J. Phys. **14**, 115001 (2012).

[17] K. Chen, B. Wang, and S. Granick, Nat. Mater. **14**, 589 (2015).

[18] Y. Yang, V. Marceau, and G. Gompper, Phys. Rev. E **82**, 031904 (2010).

[19] H. H. Wensink and H. Löwen, J. Phys.: Condens. Matter **24**, 464130 (2012); H. H. Wensink, J. Dunkel, S. Heidenreich, K. Drescher, R. E. Goldstein, H. Löwen, and J. M. Yeomans, Proc. Natl. Acad. Sci. U. S. A. **109**, 14308 (2012).

[20] T. C. Bidone, W. Jung, D. Maruri, C. Borau, R. D. Kamm, and T. Kim, PLoS Comput. Biol. **13**, 1005277 (2017).

[21] D. Grebenkov, J. Phys. A **48**, 013001 (2015).

[22] N. G. Van Kampen, *Stochastic Processes in Physics and Chemistry*, 3rd ed. (North-Holland, Amsterdam, 2007).

[23] J. Toner and Y. Tu, Phys. Rev. Lett. **75**, 4326 (1995).

[24] V. Narayan, S. Ramaswamy, and N. Menon, Science **317**, 105 (2007).

[25] S. Ramaswamy, R. A. Simha, and J. Toner, Europhys. Lett. **62**, 196 (2003).

[26] K. Husain, Ph.D thesis, National Centre for Biological Sciences, Tata Institute of Fundamental Research, 2017.

[27] X. L. Wu and A. Libchaber, Phys. Rev. Lett. **84**, 3017 (2000).

[28] M. P. Sheetz, R. Chasan, and J. A. Spudich, J. Cell. Biol. **99**, 1867 (1984).

[29] H. M. Levy, N. Sharon, and D. E. Koshland, Jr., Proc. Natl. Acad. Sci. U. S. A. **45**, 785 (1959).